Supporting Information

Sulfate modified g-C_3N_4 with enhanced photocatalytic activity towards hydrogen evolution: the role of sulfate played in photocatalysis

Yabin Jiang[a,b,‡], Zongzhao Sun[b,c,‡], Qianwen Chen[b], Yun Zhao[b], Lei Zeng[b*], Chunzhen Yang[a], Feng Huang[a], Limin Huang[b*]

[a] School of Materials, State Key Laboratory of Optoelectronic Materials and Technologies, Sun Yat-Sen University, Guangzhou 510275, P. R. China

[b] Department of Chemistry, Southern University of Science and Technology, Shenzhen, Guangdong 518055, P. R. China

[c] School of Chemistry and Chemical Engineering, Harbin Institute of Technology, Harbin 150001, P. R. China.

‡ Yabin Jiang and Zongzhao Sun equally contributed to this work.

Corresponding author:
*E-mail: zengl@sustech.edu.cn (L. Zeng)， huanglm@sustech.edu.cn (L. Huang)

Contents

Figures
Figure S1. S2p XPS spectra of $(NH_4)_2SO_4$.
Figure S2. The optimized local structures (a), the in-side positive and negative (b), the positive (c) and the negative (d) charge density distribution of CN-3H: charge accumulation is in yellow and depletion in blue. Brown, gray, yellow and red spheres represent C, N, S and O atoms, respectively
Figure S3. The optimized local structures (a), the in-side positive and negative (b), the positive (c) and the negative (d) charge density distribution of CN-3: charge accumulation is in yellow and depletion in blue. Brown, gray, yellow and red spheres represent C, N, S and O atoms, respectively
Figure S4. Powder XRD patterns of CN-3 and CN-3U.
Figure S5. S2p XPS spectra of CN-3U.
Figure S6. Photocatalytic activities for hydrogen generation over CNM, CNM-3 and CN-3 under visible light irradiation.
Figure S7. Nitrogen adsorption–desorption isotherms (a) and the corresponding pore size distribution curves (b) of CN and CN-X (X =1, 2,3,4).
Figure S8. (a) Mott−Schottky plots of CN, CN-3 and CN-3H. (b) Electronic band structure of CN, CN-3 and CN-3H. CB, conduction band; VB, valence band.
Tables
Table S1 Results of organic elemental analyses for CN, CN-X (X=1–4) and CN-3H.
Table S2 The adsorption energy analysis for the SO_4^{2-} anion adsorption on monolayer carbon nitride at site1 and site 2.
Table S3 Bader charge analysis of the monolayer carbon nitride of CN-3H and CN-3.
Table S4 Comparison of apparent quantum efficiency and activity of the CN-3 and other $g\text{-}C_3N_4$ photocatalysts reported recently in the literature.
References

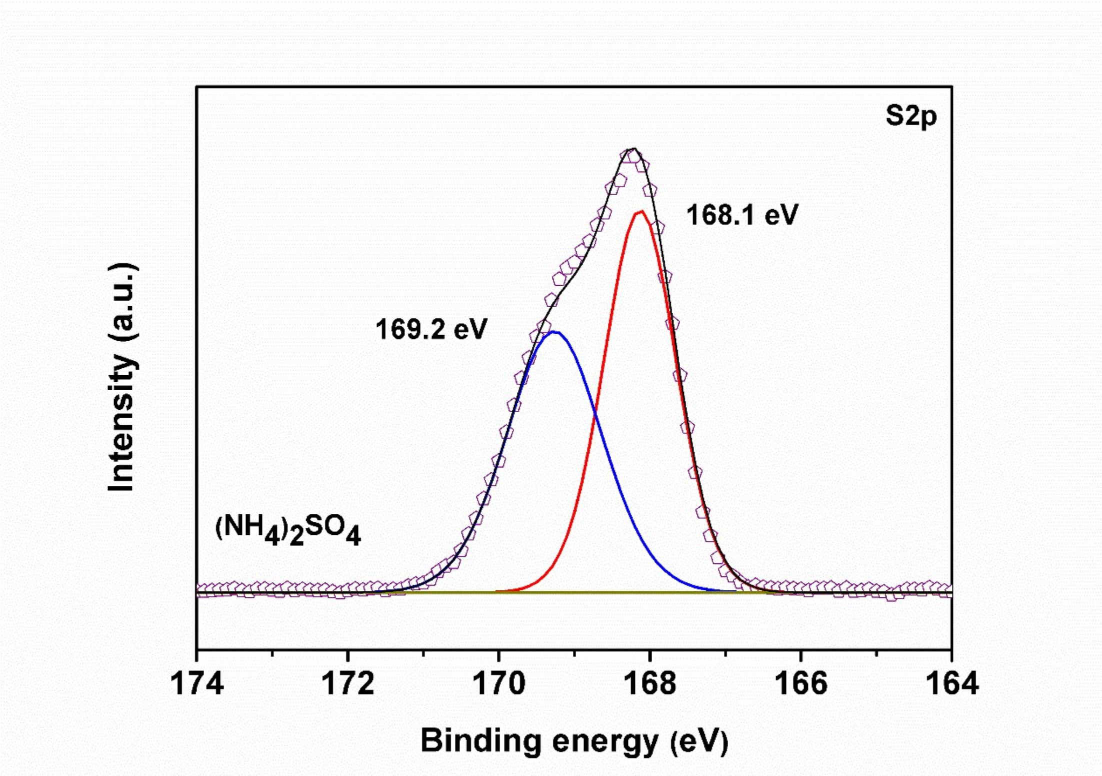

Figure S1. S2p XPS spectra of $(NH_4)_2SO_4$.

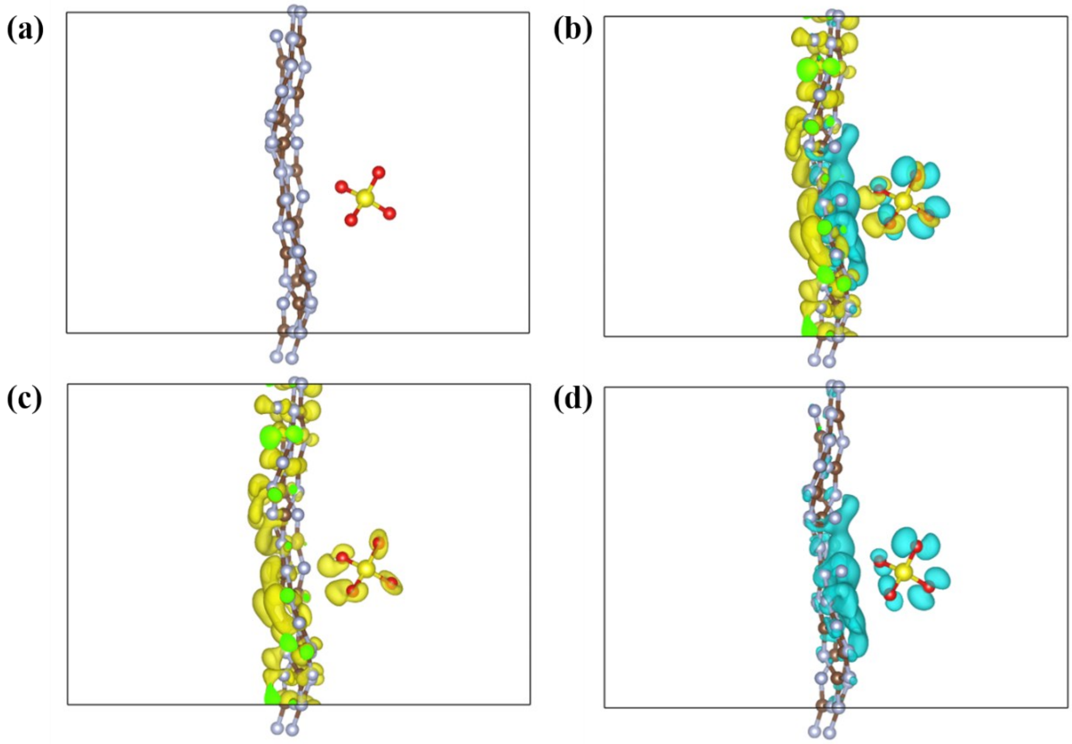

Figure S2. The optimized local structures (a), the in-side positive and negative (b), the positive (c) and the negative (d) charge density distribution of CN-3H: charge accumulation is in yellow and depletion in blue. Brown, gray, yellow and red spheres represent C, N, S and O atoms, respectively

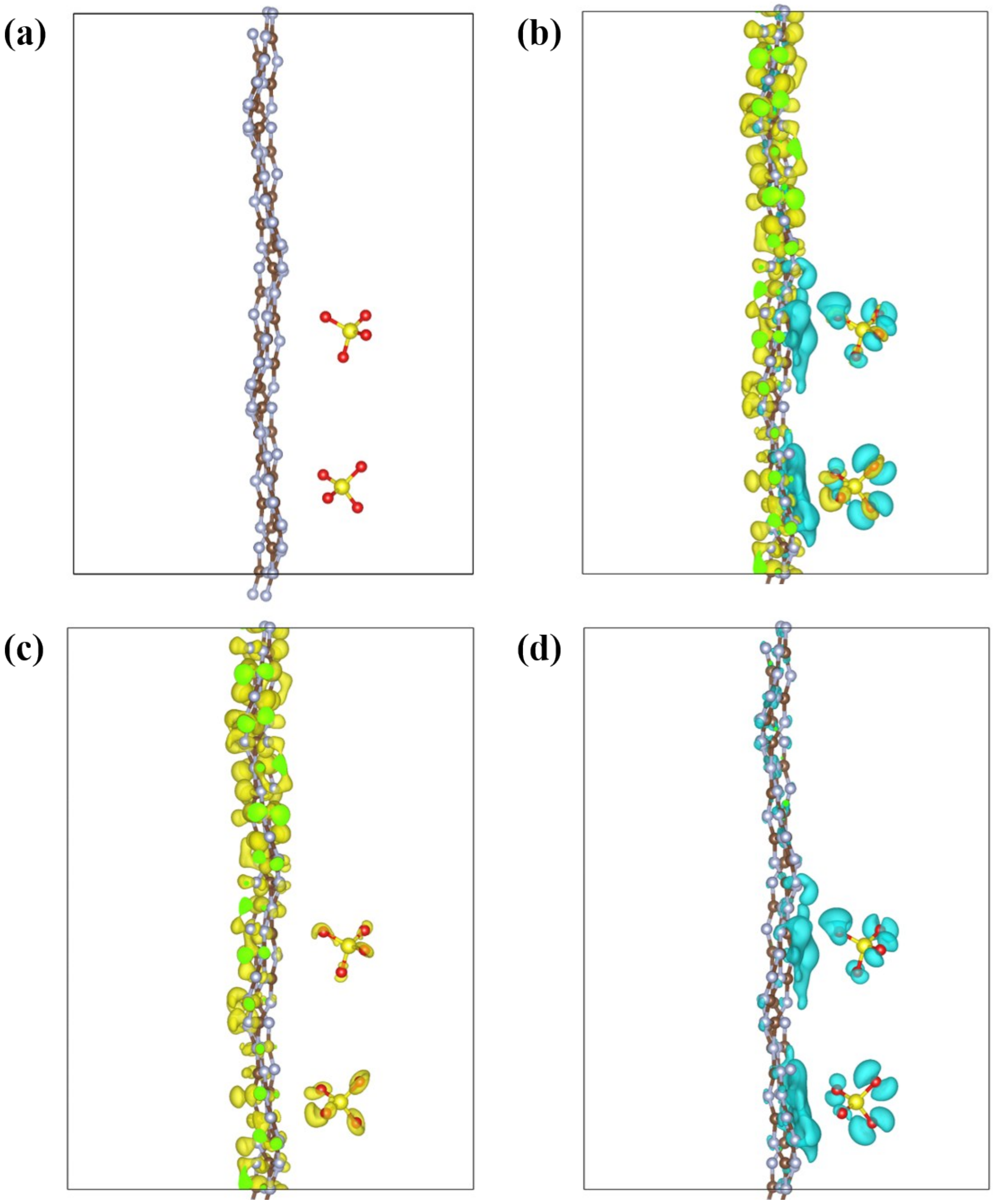

Figure S3. The optimized local structures (a), the in-side positive and negative (b), the positive (c) and the negative (d) charge density distribution of CN-3: charge accumulation is in yellow and depletion in blue. Brown, gray, yellow and red spheres represent C, N, S and O atoms, respectively

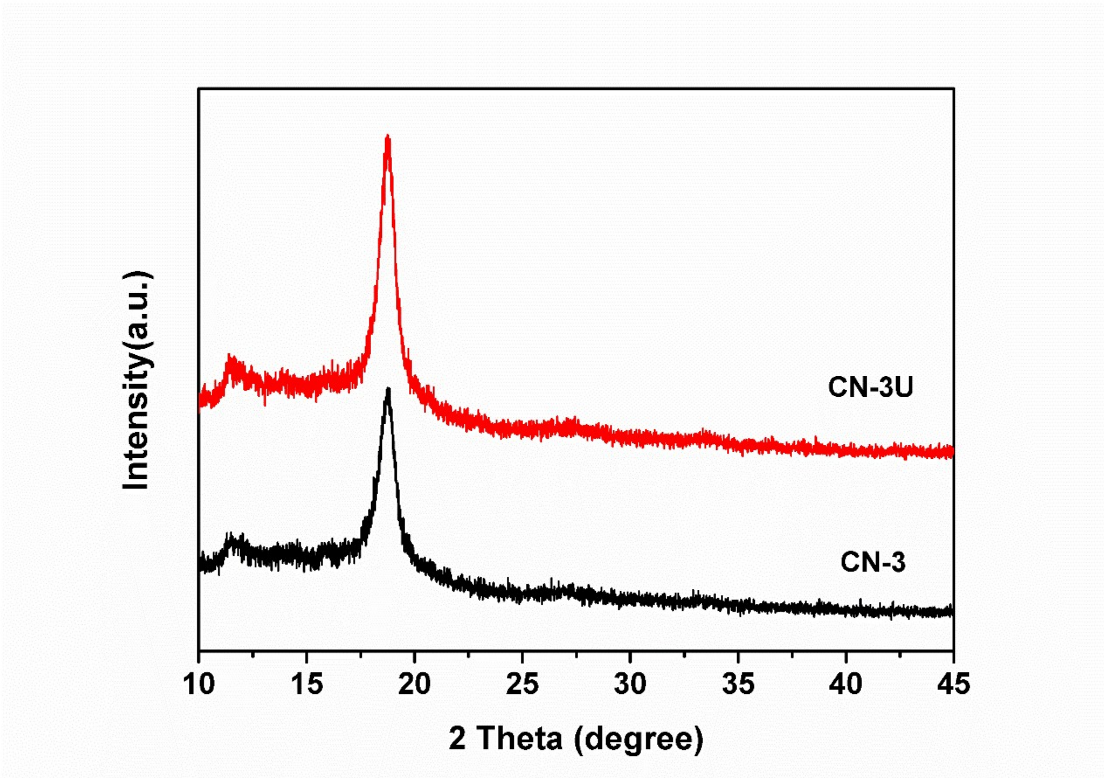

Figure S4. Powder XRD patterns of CN-3 and CN-3U.

CN-3U is the sample CN-3 after 4 consecutive cycles of reactions.

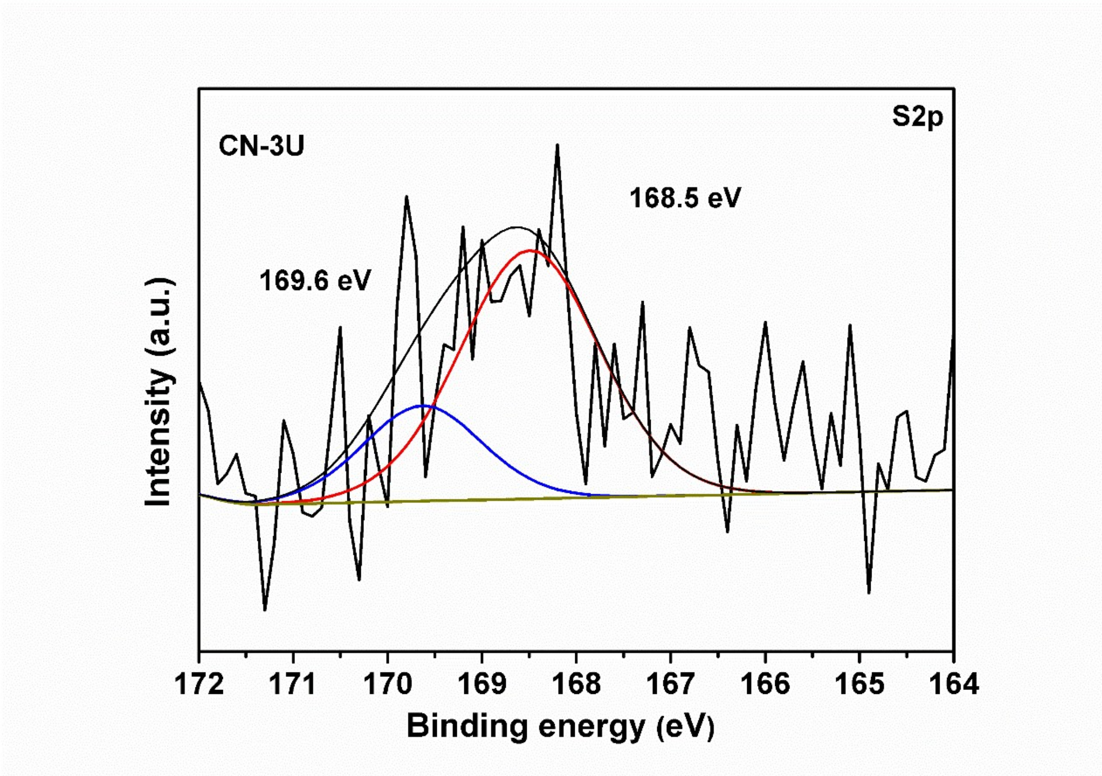

Figure S5. S2p XPS spectra of CN-3U.

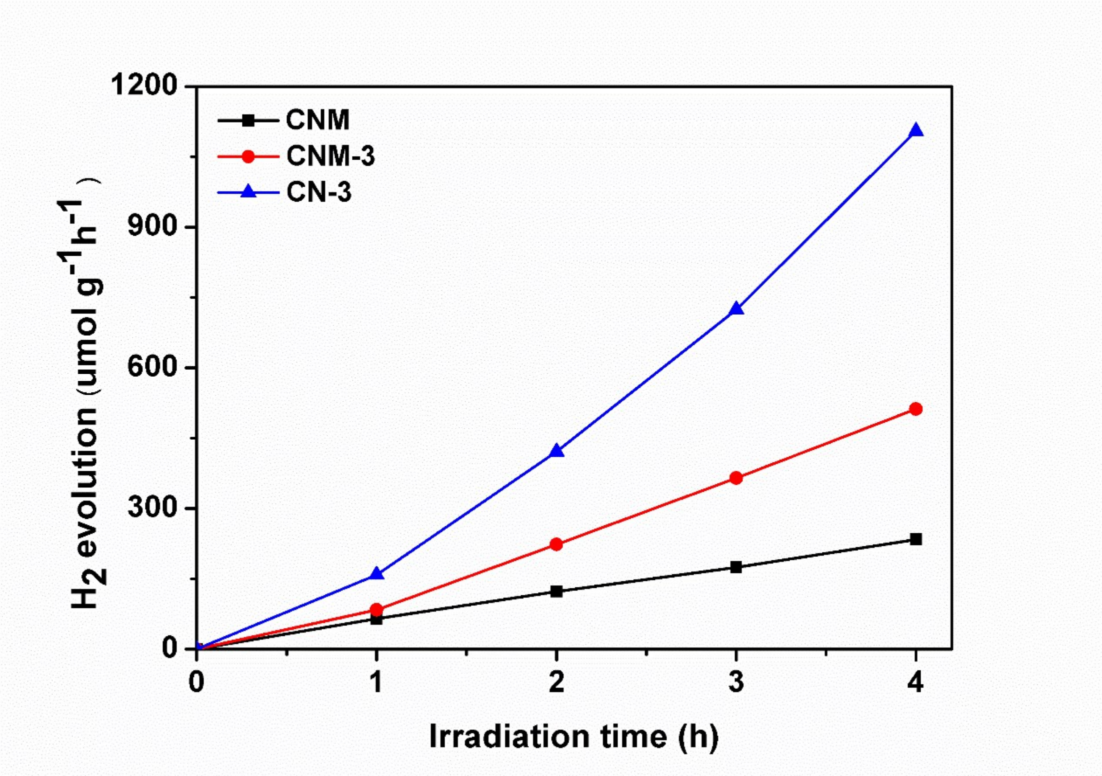

Figure S6. Photocatalytic activities for hydrogen generation over CNM, CNM-3 and CN-3 under visible light irradiation.

We also use melamine, urea and thiourea as a precursor to replace dicyandiamide to react with ammonium sulfate. It was found that only the CNM-3 can be obtained from melamine, the samples of urea and thiourea were completely decomposed. The H_2 evolution rate of CNM-3 is also better than that of CNM, but their H_2 evolution rates were lower than that of CN-3 (Figure S6), which $(NH_4)_2SO_4$ treatment improves the universality of photocatalytic performance.

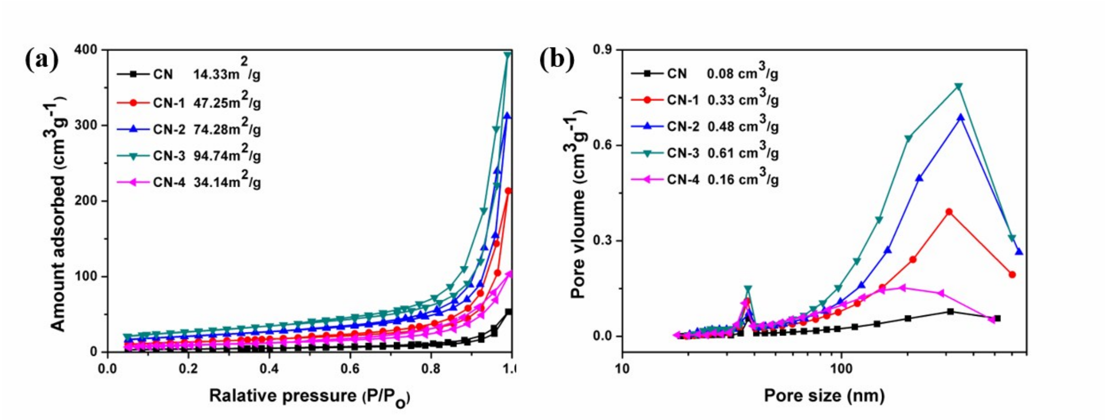

Figure S7. Nitrogen adsorption–desorption isotherms (a) and the corresponding pore size distribution curves (b) of CN and CN-X (X =1, 2,3,4).

The nitrogen adsorption–desorption isotherms and corresponding pore size distribution curves of CN and CN-X (X=1, 2, 3, 4) are provided in Figure S7. Figure S7a shows that the adsorption–desorption isotherms of all the samples are of type IV, which demonstrates the presence of mesoporous structure. When the adding amounts of $(NH_4)_2SO_4$ are below 0.75:1, the samples all show a bigger BET surface area and pore volume. However, when the amounts of $(NH_4)_2SO_4$ increased to 1: 1, the BET surface area and pore volume of the sample sharply decreased. This is because the excess introduction of $(NH_4)_2SO_4$ into the dicyandiamide-condensation reaction may change the texture and the surface morphology of the sample, e.g., collapse of mesopores, and thus decrease the surface area (ca. 34.14m^2 g^{-1}). The biggest BET surface area is 94.7 m^2 g^{-1} for CN-3 (see Figure 2), more than 6.6 times higher than that for CN (14.33 m^2 g^{-1}). Evidently, the decrease in the surface area and increase in the particle size could result in the low photocatalytic activities. Thus, the adding amount of $(NH_4)_2SO_4$ should be carefully optimized.

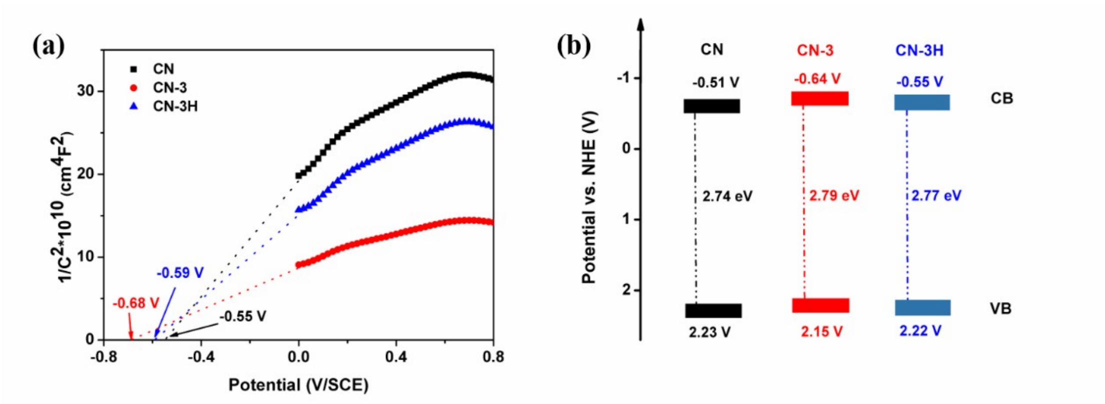

Figure S8. (a) Mott−Schottky plots of CN, CN-3 and CN-3H. (b) Electronic band structure of CN, CN-3 and CN-3H. CB, conduction band; VB, valence band.

Mott−Schottky plots (Figure S8a) can reflect the flat band potential and speculate the band energy levels. The type of semiconductor according to the positive linear slope can be estimated that CN, CN-3 and CN-3H belong to n-type characteristics. The flat band potential of CN, CN-3 and CN-3H are calculated to be -0.55, -0.68 and -0.59 V versus the saturated calomel electrode (SCE), which are equivalent to -0.31, -0.44 and -0.35 versus the normal hydrogen electrode (NHE), respectively. It is known that the conduction band position of n-type semiconductors is 0.1-0.3 eV higher than the flat potentials, depending on the electron effective mass and carrier concentration.[1] Here, the voltage difference between the conduction band and the flat potential is set to be 0.2 eV, and the bottom of the conduction band for CN, CN-3 and CN-3H are -0.51, -0.64 and -0.55V, respectively.[2] According to the above conclusion, their valence band positions can be calculated to be 2.23, 2.15 and 2.22 V, respectively. The bandgap structures of CN, CN-3 and CN-3H are depicted in Figure S8b. The apparent upshift of conduction band level can generate more electrons with stronger reducing ability and leads to a larger thermodynamic driving force in photocatalytic hydrogen production. Therefore, the conduction band position of CN-3 is more negative than CN-3H and the photocatalytic hydrogen production performance of CN-3 should be better than that of CN-3H.

Table S1 Results of organic elemental analyses for CN, CN-X (X=1–4) and CN-3H.

Sample	dicyandiamide / $(NH_4)_2SO_4$ molar ratio	C/N	N [wt%]	C [wt%]	S [wt%]	H [wt%]	O [wt%]
CN	0	0.555	59.62	33.09	0	3.249	4.041
CN-1	1/0.25	0.566	56.35	31.89	0.044	5.246	6.47
CN-2	1/0.5	0.562	56.32	31.65	0.104	6.054	5.872
CN-3	1/0.75	0.561	56.26	31.57	0.125	7.009	5.036
CN-4	1/1	0.558	55.72	30.98	0.358	5.096	7.846
CN-3H	1/0.75	0.563	54.63	30.74	0.035	4.059	10.536

Table S2 The adsorption energy analysis for the SO_4^{2-} anion adsorption on monolayer carbon nitride at site1 and site 2.

	Site1	Site2
Slab	-471.335	-471.335
A	-34.5932	-34.5932
Slab+A	-507.587	-507.04
Eads / eV	-1.65881	-1.11173

Table S3 Bader charge analysis of the monolayer carbon nitride of CN-3H and CN-3.

Sample	Bader charge/e
CN-3H	0.31
CN-3	0.76

Detailed calculation of AQY

The detail calculation of wavelength dependent apparent quantum yield is shown below:

$$\eta_{AQY} = \frac{\mathrm{N_e}}{\mathrm{N_p}} \times 100\% = \frac{2 \times M \times N_A}{\frac{E_{total}}{E_{photon}}} \times 100\%$$

$$= \frac{2M \times N_A}{\frac{S \times P \times t}{\hbar \times \frac{c}{\lambda}}} \times 100\% = \frac{2 \times M \times N_A \times \hbar \times c}{S \times P \times t \times \lambda} \times 100\%$$

Where, M represents the amount of evolved H_2 molecules (mol), N_A is the Avogadro constant (6.022×10^{23} /mol), h the Planck constant (6.626×10^{-34} J S), c the speed of light (3×10^{8} m/s), S is the irradiation area (cm^2), P the intensity of irradiation light (W/cm^2), t the photoreaction time (s), λ represents the wavelength of the incident monochromatic light (nm).

Table S4 Comparison of apparent quantum efficiency and activity of the CN-3 and other g-C_3N_4 photocatalysts reported recently in the literature.

Photocatalyst	Light source	Reaction conditions	Catalyst use (mg)	hydrogen evolution rate (μmol h^{-1})	apparent quantum efficiency	Ref.
CN-3	300 W Xe lamp, λ > 420 nm	3 wt% of $H_2PtCl_6 \cdot 6H_2O$ co-catalyst, TEOA (10%)	20	22.1	1.85% (420 nm)	This work
p-CN2	300 W Xe lamp, λ > 420 nm	3wt% of Pt co-catalyst, TEOA(20%)	50	19.8	0.79% (420 nm)	[3]
g-C_3N_4-NSs	300 W Xe lamp, λ > 420 nm	3 wt% of Pt co-catalyst, TEOA (10%)	50	493.55	N/A	[4]
Phosphorus-Doped Carbon Nitride Tubes	300 W Xe lamp, λ > 420 nm	1 wt% of Pt co-catalyst, methanol (20%)	100	67	5.68% (420 nm)	[5]
1%Au–9%SO_4 g-C_3N_4	300 W Xe lamp, λ > 400 nm	1 wt% of Au co-catalyst, TEOA (10%)	20	770	N/A	[6]
Porous Graphitic Carbon Nitride	300 W Xe lamp, λ > 420 nm	3 wt% of Pt co-catalyst, TEOA (10%)	50	99.7	N/A	[7]
Highly Crystalline Carbon Nitrides	300 W Xe lamp, λ > 420 nm	0.5 wt% of Pt co-catalyst, TEOA (15%)	20	40.5	N/A	[8]
roll-like carbon nitride	50 W LED array, λ > 410 nm	3 wt% of Pt co-catalyst, TEOA (10%)	50	22.85	N/A	[9]
Polymeric Carbon Nitride Nanoarchitectures	300 W Xe lamp, λ > 420 nm	3 wt% of Pt co-catalyst, TEOA (10%)	100	290	6.77% (455 nm)	[10]
Carbon Nitride Nanoarchitectures	300 W Xe lamp, λ > 420 nm	3 wt% of Pt co-catalyst, TEOA (10%)	50	6.1	N/A	[11]

References:

[1] W. J. Luo, Z. S. Li, X. J. Jiang, T. Yu, L. F. Liu, X. Y. Chen, J. H. Ye and Z. G. Zou, Phys. Chem. Chem. Phys., 2008, 10, 6717-6723.

[2] J. L. Wang, Y. Yu and L. Z. Zhang, Appl. Catal., B, 2013, 136– 137, 112-121.

[3] Jiang, Y., Sun, Z., Tang, C., Zhou, Y., Zeng, L., Huang, L. *Appl. Catal. B.,* 2019, **240**, 30-38.

[4] W. Iqbal, B. Qiu, J. Lei, L. Wang, J. Zhang and M. Anpo, *Dalton Trans*, 2017, **46**, 10678-10684.

[5] Guo, S., Deng, Z., Li, M., Jiang, B., Tian, C., Pan, Q., Fu, H. *Angew. Chem. Int. Ed.*, 2016, **55**, 1830-1834.

[6] S. Patnaik, S. Martha, G. Madras, K. Parida, *Phys. Chem. Chem. Phys.,* 2016, **18**,28502-28514.

[7] Li, K., Xie, X., Zhang, W. D. *ChemCatChem.,* 2016, **8**, 2128-2135.

[8] Guo, Y., Li, J., Yuan, Y., Li, L., Zhang, M., Zhou, C., Lin, Z. *Angew. Chem. Int. Ed.*, 2016, 55:14693-14697.

[9] Shalom, M., Guttentag, M., Fettkenhauer, C., Inal, S., Neher, D., Llobet, A., Antonietti, M. *Chem. Mater.,* 2014, **26,** 5812-5818.

[10] Zhang, J., Guo, F., Wang, X. *Adv. Funct. Mater.,* 2013, **23**, 3008-3014.

[11] Cui, Y., Ding, Z., Fu, X., Wang, X. *Angew. Chem. Int. Ed.*, 2012, **51**, 11814-11818